Manipulation of two-photon-induced fluorescence spectra of chromophore aggregates with entangled photons: A simulation study

Frank Schlawin, Konstantin E. Dorfman, Benjamin P. Fingerhut, and Shaul Mukamel*
Department of Chemistry, University of California, Irvine, California 92697-2025, USA
(Received 19 April 2012; published 29 August 2012)

The nonclassical spectral and temporal features of entangled photons offer new possibilities to investigate the interactions of excitons in photosynthetic complexes and to target the excitation of specific states. Simulations of fluorescence in the bacterial reaction center induced by entangled light demonstrate a degree of selectivity of double-exciton states which is not possible using classical stochastic light with the same power spectrum.

DOI: 10.1103/PhysRevA.86.023851 PACS number(s): 42.62.Fi, 78.47.jh, 42.65.Lm

I. INTRODUCTION

Apart from their evident importance in experimental tests of the foundations of quantum mechanics, entangled photons promise many applications to quantum information processing [1,2], secure quantum communication [3–5], lithography [6–9], or metrology [10–12]. In addition, their nonclassical frequency and time correlations could also open up novel spectroscopic applications [13,14]. Entanglement-induced two-photon transparency [15] and the linear scaling of two-photon-induced fluorescence with the pump intensity [16] constitute two basic nonclassical effects observed with entangled photon pairs. This scaling makes it possible to carry out nonlinear optical measurements with much lower light intensity compared to classical light, as we will discuss in Sec. III. More generally, entangled photons offer new control parameters for nonlinear spectroscopy [17] and can be used to distinguish quantum pathways of matter [18]. It remains, however, an open question to what extent quantum entanglement is essential for these effects and whether some can be reproduced, for instance, by shaped or stochastic classical pulses [19,20]. Recently, it has been argued that entanglement can induce collective resonances between noninteracting two-level atoms [21]. It was later found that these resonances may not be observed in fluorescence due to destructive interference of pathways [13].

In this paper we present a theoretical framework for describing excitations induced by entangled photons in chromophore aggregates. These possess manifolds of single- and double-exciton states [22], and the excitation of each double-exciton state can take place via many interfering pathways (see Fig. 1). We show that the nonclassical spectral and temporal properties of twin photons can be used to excite state distributions that may not be obtained by classical light. Due to energy conservation in their generation, the sum of the energies of twin photons $\omega_p = \omega_1 + \omega_2$ has a sharp distribution (i.e., $\Delta\omega_p$ is very small), even though each single photon may be broadband ($\Delta\omega_1, \Delta\omega_2$ very large). The high frequency resolution of ω_p allows us to target certain double-exciton states, while the broad bandwidth of the individual beams enables the simultaneous access of all possible pathways that reach the double-exciton state (see Fig. 1). In contrast, with classical fields the bandwidths of the two beams add up and create a large uncertainty in the sum. Our simulations show that the nonclassical distributions could be detected by the fluorescence signal. The control parameters of the entangled light can be used to stretch the signal in two-dimensional plots, which could reveal additional information about the matter.

II. THE MODEL

We consider a chromophore aggregate interacting with the electromagnetic field and described by the Hamiltonian

$$H = H_0 + H_F + H_{\text{int}}, \tag{1}$$

where H_0, H_F, and H_{int} represent the aggregate, the field, and their coupling, respectively. The electronic states group into well-separated manifolds, which are denoted as e manifold (single-exciton), f manifold (double-exciton), etc. The field couples to the system via the dipole operator, which induces transitions between these manifolds. In the rotating-wave approximation, the interaction Hamiltonian reads

$$H_{\text{int}}(t) = V(t)E^\dagger(t) + V^\dagger(t)E(t), \tag{2}$$

where we have introduced the positive-frequency component of the dipole operator,

$$V(t) = \sum_e (\mu_{eg}|g\rangle\langle e|e^{-i\omega_{eg}t} + \sum_f \mu_{fe}|e\rangle\langle f|e^{-i\omega_{fe}t}), \tag{3}$$

in which $\omega_{ij} = (E_i - E_j)/\hbar$ are matter transition frequencies and μ_{ij} are the dipole moments. The corresponding negative-frequency part of the electromagnetic field operator is given by

$$E^\dagger(t) = \sum_s \left(\frac{2\pi\omega_s}{\Omega}\right)^{1/2} a_s^\dagger e^{i\omega_s t}, \tag{4}$$

where Ω denotes the quantization volume, $a_s^\dagger$ is the creation operator for mode s, and s runs over the relevant modes. Assuming perfect phase matching, we can neglect the spatial dependencies of the electromagnetic field. This is justified for large samples. Coupling with a phonon bath can induce many interesting relaxation effects. These are not included in the present study. We first derive general expressions for density-matrix elements in the single- and the double-exciton manifolds in terms of convolutions of matter- and field-correlation functions. These results are valid for light with arbitrary statistical properties and can describe two-photon-induced fluorescence and related measurements in a consistent

*smukamel@uci.edu

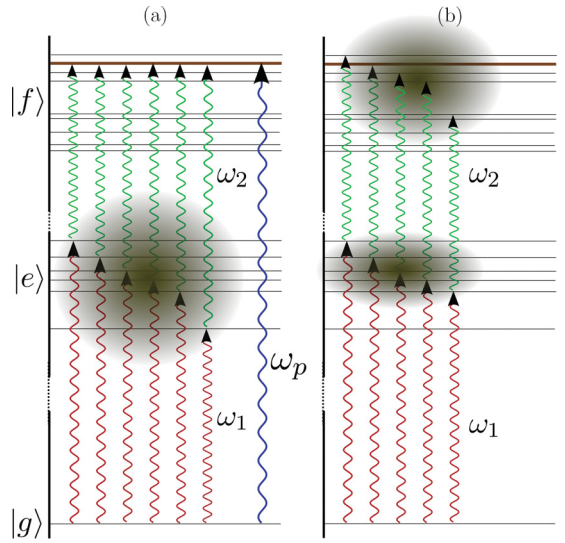

FIG. 1. (Color online) (a) Two-photon transitions with entangled photons. The broad bandwidth allows us to access the entire manifold $|e\rangle$; at the same time the manifold $|f\rangle$ is well resolved due to the narrow distribution of $\omega_1+\omega_2$. (b) Transitions with classical light. Bandwidths of ω_1 and ω_2 now add up, and the f manifold cannot be resolved.

manner. The matrix element (e_i,e_j) of the single-exciton block of the density matrix is given by

$$\varrho_{e_ie_j}(t)=\mathrm{tr}[|e_j(t)\rangle\langle e_i(t)|\varrho(t)], \tag{5}$$

where $\varrho(t)$ denotes the density matrix of the entire matter-field system. In a superoperator Liouville space representation, the formal solution of the Heisenberg equation is given by the Dyson series [23]

$$\varrho(t)=\mathcal{T}\exp\left(-\frac{i}{\hbar}\int^t d\tau H_{\mathrm{int},-}(\tau)\right)\varrho(-\infty), \tag{6}$$

where $\mathcal{T}$ is the time-ordering operator, and the superoperator $H_{\mathrm{int},-}$ is defined through $A_-\varrho=A\varrho-\varrho A$ in the interaction picture with respect to H_0+H_F. For weak fields we can expand the exponential, and the leading (second) order contribution to Eq. (5) yields

$$\varrho'_{e_ie_j}(t;\Gamma)=-\left(-\frac{i}{\hbar}\right)^2\int_{-\infty}^t d\tau_1\int_{-\infty}^t d\tau_2 \times\left\langle V(\tau_2)A_{ij}(t)V^\dagger(\tau_1)\right\rangle\langle E^\dagger(\tau_2)E(\tau_1)\rangle, \tag{7}$$

where $A_{ij}(t)\equiv|e_j(t)\rangle\langle e_i(t)|$ and Γ denotes the set of control parameters that govern the excitation, e.g., frequencies, pulse envelopes, etc. The angle brackets $\langle\cdots\rangle$ denote the quantum-mechanical expectation value with respect to the initial state $\varrho(-\infty)$,

$$\varrho(-\infty)=|g\rangle\langle g|\otimes\varrho_{\mathrm{field}}, \tag{8}$$

i.e., the aggregate is in the ground state $|g\rangle$, and the electromagnetic field is prepared in a state ϱ_{field}.

The fourth-order processes that end in the $|e\rangle$ manifold can be represented by diagrams I and II in Fig. 2 (for diagram rules, see [24]). These can be divided into two classes: Raman type that only involve single-exciton resonances (diagram I) and two-photon absorption type (diagram II) that involve the double-exciton manifold. We have to take two additional diagrams into account, in which three interactions occur on the right-hand side. Apart from the projector $|e_j(t)\rangle\langle e_i(t)|$, these are simply the complex conjugates of diagrams I and II in Fig. 2. We can thus write them as

$$\begin{aligned}\varrho_{e_ie_j,\mathrm{I}}(t;\Gamma)=-\left(-\frac{i}{\hbar}\right)^4\int_{-\infty}^t d\tau_4\int_{-\infty}^t d\tau_3\int_{-\infty}^{\tau_3} d\tau_2\int_{-\infty}^{\tau_2} d\tau_1 \\ \times[\langle V(\tau_4)A_{ij}(t)V^\dagger(\tau_3)V(\tau_2)V^\dagger(\tau_1)\rangle \\ \times\langle E^\dagger(\tau_4)E(\tau_3)E^\dagger(\tau_2)E(\tau_1)\rangle \\ +\langle V(\tau_1)V^\dagger(\tau_2)V(\tau_3)A_{ij}(t)V^\dagger(\tau_4)\rangle \\ \times\langle E^\dagger(\tau_1)E(\tau_2)E^\dagger(\tau_3)E(\tau_4)\rangle]\end{aligned} \tag{9}$$

$$\begin{aligned}\varrho_{e_ie_j,\mathrm{II}}(t;\Gamma)=-\left(-\frac{i}{\hbar}\right)^4\int_{-\infty}^t d\tau_4\int_{-\infty}^t d\tau_3\int_{-\infty}^{\tau_3} d\tau_2\int_{-\infty}^{\tau_2} d\tau_1 \\ \times[\langle V(\tau_4)A_{ij}(t)V(\tau_3)V^\dagger(\tau_2)V^\dagger(\tau_1)\rangle \\ \times\langle E^\dagger(\tau_4)E^\dagger(\tau_3)E(\tau_2)E(\tau_1)\rangle \\ +\langle V(\tau_1)V(\tau_2)V^\dagger(\tau_3)A_{ij}(t)V^\dagger(\tau_4)\rangle \\ \times\langle E^\dagger(\tau_1)E^\dagger(\tau_2)E(\tau_3)E(\tau_4)\rangle].\end{aligned} \tag{10}$$

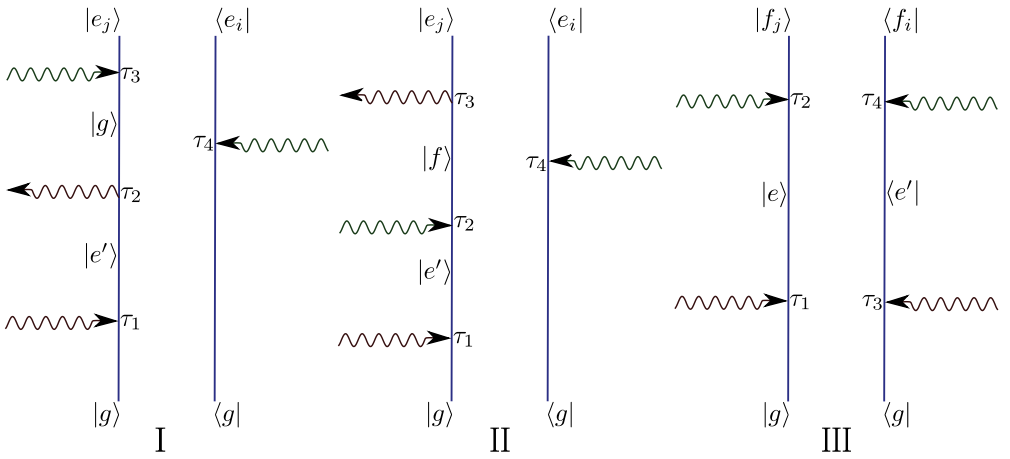

FIG. 2. (Color online) Diagrams I and II: the single-exciton density matrix. Diagram III: the two-exciton density matrix.

Note that for diagonal density-matrix elements, i.e., $e_i = e_j$, we can combine the two terms in both (9) and (10) and recast them as the real part of the first term. To the same order, double-exciton matrix elements are given by diagram III of Fig. 2,

$$\varrho_{f_i f_j,\mathrm{III}}(t;\Gamma) = \left(\frac{i}{\hbar}\right)^4 \int_{-\infty}^{t} d\tau_4 \int_{-\infty}^{\tau_4} d\tau_3 \int^{t} d\tau_2 \int^{\tau_2} d\tau_1 \times \langle V(\tau_3) V(\tau_4) B_{ij}(t) V^\dagger(\tau_2) V^\dagger(\tau_1)\rangle \times \langle E^\dagger(\tau_3) E^\dagger(\tau_4) E(\tau_2) E(\tau_1)\rangle, \quad (11)$$

where $B_{ij}(t) \equiv |f_j(t)\rangle\langle f_i(t)|$. Equations (9)–(11) enable us to evaluate the density matrix for arbitrary states of the radiation field once we specify its four-point field correlation function.

III. LIGHT SOURCES

A. The twin-photon state

Extensive research effort has focused on producing and detecting pairs of entangled photons. Numerous schemes have been employed for the generation of entangled photon pairs, including parametric down conversion [25], biexciton decay in semiconductors [26,27], or four wave mixing in optical fibers [28,29].

We consider a type of entangled light known as twin photons [30]. It is created by type-II parametric down conversion with a cw-pump laser of frequency ω_p. When the pump beam is sufficiently weak, it predominantly produces temporally nonoverlapping pairs of entangled photons. The state of the field can then be obtained perturbatively in the interaction Hamiltonian of the pump beam with the nonlinear crystal [30],

$$|\psi\rangle = E_p \int d\vec{k}_1 \int d\vec{k}_2 \, \mathrm{sinc}[(k_p - k_{1z} - k_{2z})L/2] \times e^{i(k_p - k_{1z} - k_{2z})L/2} \delta(k_{1x} + k_{2x}) \, \delta(k_{1y} + k_{2y}) \times \delta[\omega(\vec{k}_1) + \omega(\vec{k}_2) - \omega_p] |\vec{k}_1 \vec{k}_2\rangle, \quad (12)$$

where E_p is the pump field amplitude. The state is not normalized. Here, the length of the crystal along the pump beam is denoted L, while it is assumed to be infinitely large in the other two directions. In the setup depicted in Fig. 3, one collects the light in two outgoing directions, θ_1 and θ_2, with respect to the optical axis, thus fixing the central frequencies

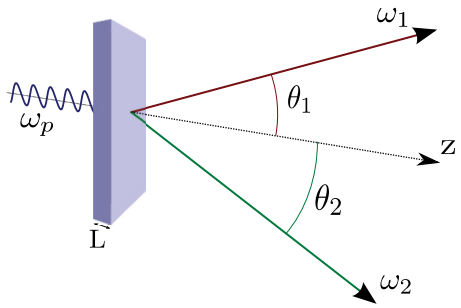

FIG. 3. (Color online) Parametric down-conversion setup to produce twin photons: A high-energy pump of frequency ω_p creates two beams of entangled photons with central frequencies ω_1 and ω_2, such that $\omega_p = \omega_1 + \omega_2$. The central frequencies are determined by the relative angles between the direction of propagation.

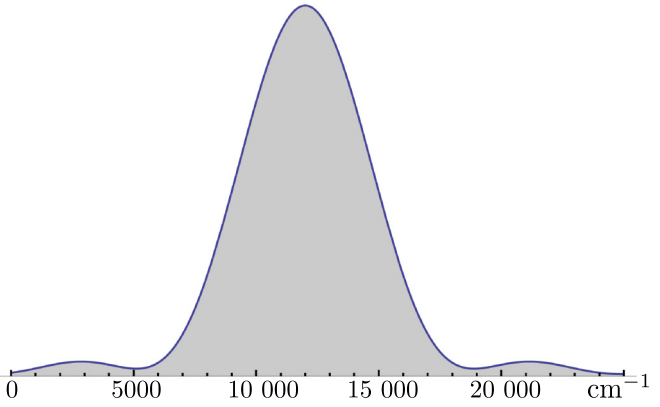

FIG. 4. (Color online) Power spectrum of entangled light [Eq. (13)] with $T = 30$ fs. The central frequencies are $\omega_1 = 13\,000$ cm^{-1} and $\omega_2 = 11\,000$ cm^{-1}. The two sinc^2 functions overlap to form a single broad peak.

ω_1 and ω_2 of the photon wave packets in directions 1 and 2. Moreover, the photon pairs are correlated in time. This is characterized by the entanglement time T, which is determined by the length L along the axis of the pump beam and group velocity dispersion inside the crystal. Therefore, one can vary independently T and two of the three frequencies ω_p, ω_1, and ω_2.

For short T, Eq. (12) leads to the broad power spectrum

$$n_{\mathrm{twin}}(\omega) = \int_{-\infty}^{\infty} dt_1 dt_2 e^{-i\omega(t_1 - t_2)} \langle E^\dagger(t_1) E(t_2)\rangle = n_0 |E_p|^2 \left(\mathrm{sinc}^2 \left[\frac{(\omega - \omega_1)T}{2}\right] + \mathrm{sinc}^2 \left[\frac{(\omega - \omega_2)T}{2}\right]\right), \quad (13)$$

which is depicted in Fig. 4. To evaluate the normally ordered correlation functions in Eq. (10), we note that it can be separated into

$$\langle E^\dagger(\tau_3) E^\dagger(\tau_4) E(\tau_2) E(\tau_1)\rangle = \langle \psi | E^\dagger(\tau_3) E^\dagger(\tau_4) |0\rangle \langle 0 | E(\tau_2) E(\tau_1) | \psi\rangle, \quad (14)$$

where [30]

$$\langle 0 | E(\tau_2) E(\tau_1) | \psi\rangle = C E_p \, \mathrm{rect}\left(\frac{\tau_2 - \tau_1}{T}\right) (e^{-i\omega_1\tau_1 - i\omega_2\tau_2} + e^{-i\omega_1\tau_2 - i\omega_2\tau_1}). \quad (15)$$

Here, C is a constant and we have defined the rectangular function

$$\mathrm{rect}(x) = \begin{cases} 1 & \text{for} \quad x < 1, \\ 0 & \text{otherwise.} \end{cases} \quad (16)$$

The nonclassical nature of the quantum state produced by this setup has been verified in numerous experiments [31–38]. One important feature that follows from Eqs. (14) and (15) is that the four-point correlation function of the fields scales linearly with the pump intensity $|E_p|^2$, while classically it scales quadratically [39]. This scaling behavior can be utilized in

experiments to determine intensity regimes, in which Eq. (12) can account for the produced signal. In practice, we expect this linear scaling of fourth-order signals with a crossover to a quadratic classical scaling at higher intensities. The light beam can be considered to be made of pairs of photons. At weak intensities the pairs are temporally well separated, and the process is induced by two photons of the same pair. At higher intensities it becomes statistically more plausible for the two photons to come from different pairs, which are not entangled, and the classical scaling is recovered. This crossover has been demonstrated experimentally [35–38]. For instance, in Ref. [35] the authors detect it at an intensity (of the entangled photon flux) of 1.5 μW in a periodically poled potassium titanyl phosphate crystal, which was obtained by a pump intensity of less than 2.5 W. The linear scaling of the two-photon absorption was also demonstrated experimentally for organic porphyrin dendrimers [36,37].

Entangled photon sources are weak, but at the same time weak intensities are required to see the effect of entanglement. Nonlinear spectroscopy and imaging with weak fields should allow us to limit the damage to biological samples.

B. Stochastic light with the same power spectrum

To highlight the effects of entanglement, we consider a classical reference state of the field with the same power spectrum. To that end, we introduce the frequency decomposition of a classical field,

$$E_i(t) = \sum_i \int d\omega\ A_i(\omega)\ e^{-i\omega t - i\phi(\omega)}, \tag{17}$$

where A_i and ϕ_i are real functions representing the amplitude and the phase of the various modes. To reproduce the power spectrum, Eq. (13), we took

$$A_1(\omega) = A_0\ \mathrm{sinc}[(\omega-\omega_1)T/2]e^{-i\phi(\omega)}, \tag{18}$$

$$A_2(\omega) = A_0\ \mathrm{sinc}[(\omega-\omega_2)T/2]e^{-i[\phi(\omega)+\pi/2]}. \tag{19}$$

With this choice $\phi(\omega)$ does not affect the power spectrum and will be chosen to obtain stationary stochastic light (rather than a pulse). We assume that $\phi(\omega)$ is a random function, so there is no well-defined phase relation between the different frequencies. The quantum-mechanical expectation value in correlation functions such as $\langle E^\dagger(\tau_3)E^\dagger(\tau_4)E(\tau_2)E(\tau_1)\rangle$ then needs to be replaced by an average over the distribution of $\phi(\omega)$:

$$\begin{aligned}&\langle E^\dagger(\tau_3)E^\dagger(\tau_4)E(\tau_2)E(\tau_1)\rangle\\ &\quad= \int d\omega_1' \int d\omega_2' \int d\omega_3' \int d\omega_4'\ A(\omega_1')A(\omega_2')\\ &\qquad\times A^*(\omega_3')A^*(\omega_4')e^{-i(\omega_2'\tau_2+\omega_1'\tau_1)}e^{i(\omega_4'\tau_4+\omega_3'\tau_3)}\\ &\qquad\times \int d\phi(\omega)\ e^{-i[\phi(\omega_1')+\phi(\omega_2')-\phi(\omega_3')-\phi(\omega_4')]}.\end{aligned} \tag{20}$$

Assuming that ϕ is uniformly distributed in the interval $[0,2\pi)$, we find that E is a stationary Gaussian process:

$$\begin{aligned}\langle E^\dagger(\tau_3)E^\dagger(\tau_4)E(\tau_2)E(\tau_1)\rangle &= \langle E^\dagger(\tau_3)E(\tau_2)\rangle\langle E^\dagger(\tau_4)E(\tau_1)\rangle\\ &\quad+\langle E^\dagger(\tau_4)E(\tau_2)\rangle\langle E^\dagger(\tau_3)E(\tau_1)\rangle.\end{aligned} \tag{21}$$

Thus, classical light only shows correlations on the level of intensities, i.e., $\langle E^\dagger E\rangle$. By substitution of Eqs. (18) and (19) we then obtain

$$\begin{aligned}&\langle E^\dagger(\tau_3)E^\dagger(\tau_4)E(\tau_2)E(\tau_1)\rangle\\ &\quad= \mathcal{N}\sum_{\omega_a,\omega_b}\left[\mathrm{tri}\left(\frac{\tau_1-\tau_3}{T}\right)\mathrm{tri}\left(\frac{\tau_2-\tau_4}{T}\right)\right.\\ &\qquad\times e^{-i\omega_a(\tau_1-\tau_3)}e^{-i\omega_b(\tau_2-\tau_4)} + \mathrm{tri}\left(\frac{\tau_1-\tau_4}{T}\right)\mathrm{tri}\left(\frac{\tau_2-\tau_3}{T}\right)\\ &\qquad\left.\times e^{-i\omega_a(\tau_1-\tau_4)}e^{-i\omega_b(\tau_2-\tau_3)}\right],\end{aligned} \tag{22}$$

where the summations run over ω_1 and ω_2 and tri(x) is the triangular function as defined in Eq. (A2). This correlation function represents stationary, stochastic light since it only depends on time differences, just like the one produced by entangled photons with a stationary pump [see Eq. (15)]. However, there is one crucial difference. The quantum-mechanical expectation value can be factorized in Eq. (14) and only depends on $\tau_3-\tau_4$ and $\tau_2-\tau_1$. The correlation function (22) depends on $\tau_1-\tau_3$, $\tau_2-\tau_4$, $\tau_1-\tau_4$, and $\tau_2-\tau_3$.

IV. SINGLE- AND DOUBLE-EXCITON DENSITY MATRICES IN THE BACTERIAL REACTION CENTER

We now present simulations of the exciton density matrices produced by entangled and stochastic light with the same spectral density in a model of the bacterial reaction center (RC) of purple bacteria *Blastochloris viridis* [41]. The primary steps in photosynthesis involve excitation energy transfer towards and charge separation within RCs. The RC of purple bacteria utilizes the high-intensity near-IR region of the solar irradiation and transforms the energy into a chemical potential gradient with near-unity efficiency. In bacterial RC the charge separation occurs in the active branch of the protein on the subpicosecond to low-picosecond time scale [42,43]. The quenching of the excited-state special pair population has been demonstrated experimentally in time-resolved emission measurements [44,45].

The electronic Hamiltonian H_0 describes the optically bright chromophore excitations and dark charge-separated states in the active branch of the RC in a tight-binding formulation. It includes 12 single- and 41 double-exciton states, as depicted in Fig. 5(c). To construct H_0, we start with the x-ray structural data for *B. viridis* (Protein Data Bank code: 1PRC) [40]. The Q_y transition dipole moments are placed at the center of bacteriochlorophylls (BCls) and bacteriopheophytins (BPs). The excitation energies of BCls and BPs are taken from Ref. [46], Förster couplings are calculated in the dipole approximation, except for the special pair where a value of 852 cm^{-1} was chosen, allowing us to reproduce the circular dichroisim spectra of *B. viridis*. The energy of the primary charge-separated (CS) state is fixed relative to the lowest special pair exciton state [47,48], which yields a reference point for the additional CS energies of the active branch. The Hamiltonian is given in detail in Ref. [41]. Dephasing effects and incoherent population transport were neglected. To model the absorption spectrum shown in Fig. 5, we assume the same lifetime broadening $\gamma = 200$ cm^{-1}

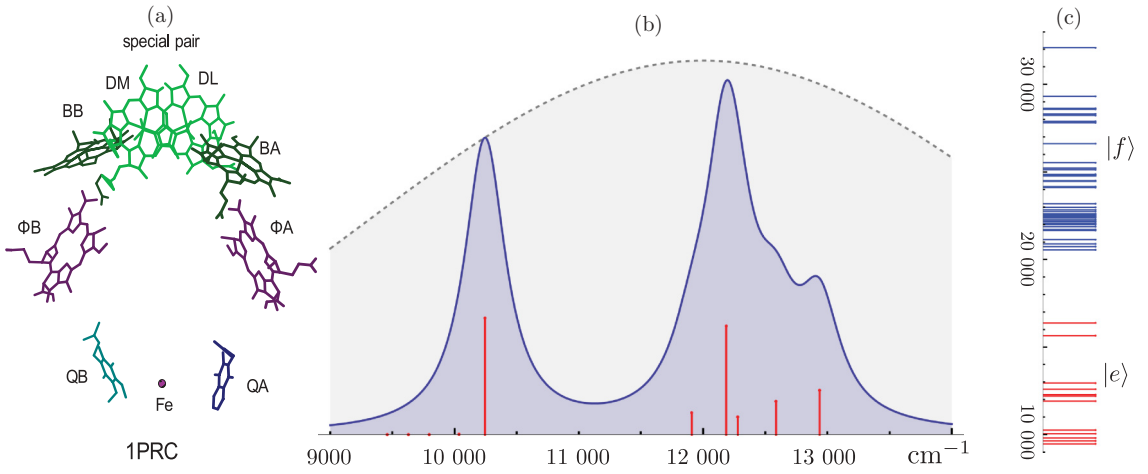

FIG. 5. (Color online) (a) Arrangement of the six chromophores of the bacterial RC (Protein Data Bank code: 1PRC) [40]. (b) The absorption spectrum of the RC. The lifetime broadening of the excited states is taken to be 200 cm^{-1}. The gray dashed line shows the power spectrum of Fig. 4, the single exciton states are indicated by red lines, and their heights are proportional to their transition dipole moments $|\mu_{ge}|^2$. (c) Level scheme of the RC. The 12 single-exciton states are marked in red, and the 41 double-exciton states in blue.

for all single-exciton states, which agrees reasonably with more detailed simulations [41]. In Fig. 5(b), we mark the single-exciton states e by vertical lines, whose length is proportional to their oscillator strength $|\mu_{ge}|^2$. The spectrum is dominated by six states corresponding to molecular Frenkel excitations of the constituents of the RC. The other six charge transfer states are dark and cannot be accessed spectroscopically.

The exciton density matrix induced by entangled or stochastic light is block diagonal in the e and f manifolds since a coherence between the two manifolds can be related to field correlation functions of the kind $\langle E^\dagger E^\dagger E\rangle$ or $\langle E^\dagger E E\rangle$, which vanish for any Fock state or stationary Gaussian process. In Fig. 6 we depict the absolute values of the density-matrix elements of the double-exciton states f_{10} to f_{30} for $\omega_p = 22\,160$ and 24 200 cm^{-1}. Entangled light excites a pure double-exciton

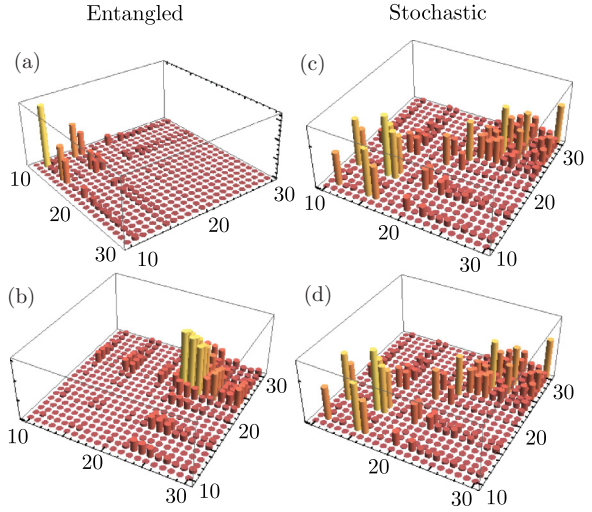

FIG. 6. (Color online) The double-exciton manifold density matrix upon excitation by entangled light with (a) $\omega_p = 22160$ cm^{-1} and (b) 24200 cm^{-1}. (c) and (d) The same as (a) and (b), but for stochastic light. Only the dominant states $f_{10} \cdots f_{30}$ are shown.

state, $\sum_f T_{fg}(t)|f\rangle$ [see Eq. (A8)]. Consequently, the purity of the density matrices in Figs. 6(a) and 6(b) is $\mathrm{tr}_f\{\varrho_f^2\} = 1$. The density matrix induced by stochastic light [Figs. 6(c) and 6(d)] is not in a pure state; we obtain $\mathrm{tr}_f\{\varrho_f^2\} \approx 0.24$ independent of the pump frequency. Furthermore, it is apparent that by tuning the pump frequency, we can select the excitation of certain states. Figure 6(a) shows strong excitation of states f_{11}, f_{15}, and f_{16}, while in Fig. 6(b) the states between f_{27} and f_{30} are most strongly excited. This selectivity allows us to manipulate of the fluorescence signal, as will be shown in the next section. While the density matrices in Figs. 6(a) and 6(b) strongly depend on the pump frequency, our calculations of the corresponding density matrices produced by stochastic light indicate no such selectivity. The results are plotted in Figs. 6(c) and 6(d). For both pump frequencies ($\omega_1 + \omega_2 = 22\,160$ and 24 200 cm^{-1}), the excitation is distributed among the bright states $f_{11}, f_{15}, f_{22}, f_{25}, f_{27}$, and f_{30}.

Figure 7 shows the single-exciton manifold density matrices [Eq. (A5)] for the same pump frequencies 22 160 and 24 200 cm^{-1}. Our results qualitatively resemble the ones for the double-exciton manifold. By varying ω_p we can enhance [Fig. 7(a)] or suppress [Fig. 7(b)] the excitation of e_5 (and, vice versa, of e_6 and e_7), while stochastic light always creates very similar density matrices. For both frequencies, the population is mainly distributed between states e_5 and e_7.

The total population of the single-exciton manifold $\sum_e \varrho'_{ee}$ calculated to second order in the matter-field interaction [Eq. (A3)] is displayed in Fig. 8 vs the frequencies ω_p and ω_2. Due to the broadband nature of the beams, none of the peaks of the absorption spectrum in Fig. 5(b) can be resolved. This population only depends on the spectral density, is identical for stochastic and entangled light, and is not susceptible for the nonclassical features of entangled light.

The total double-exciton population $\sum_f \varrho_{ff}$ created by Eq. (A8) is plotted in Fig. 9(a). The distribution of the single-exciton states to fourth order (see diagram II in Fig. 2) looks almost identical since Eq. (10) includes an excitation to the double-exciton manifold, and it is not shown. It depends only

weakly on ω_2, reflecting the energy uncertainty due to the time entanglement. Thus, the central frequency of each beam is not important, and in the following we set $\omega_2 = 11\,000\ \mathrm{cm}^{-1}$. Two broad resonance bands, at 22 000–23 000 cm^{-1} (band a) and at 23 000–24 000 cm^{-1} (band b), dominate the distribution. From our previous discussion of the density matrix, we anticipate that states f_{11}, f_{15}, and f_{16} dominate band a, whereas states f_{23}–f_{27} seem to make up band b (see Fig. 6). The signal induced by stochastic light [Fig. 9(b)] shows no such structure. Due to the broad bandwidth, the level structure of the RC cannot be resolved at all.

To get a more detailed picture of this state distribution, we depict the contribution of various double-exciton state populations to the distribution [Eq. (A8)] in Fig. 10(a). The distributions are normalized at each ω_p. States f_{11}, f_{15}, and f_{16} dominate band a, whereas band b is dominated by states f_{23}, f_{24}, and f_{25}. At higher pump frequency, states f_{27}, f_{30}, and f_{32} are the most pronounced. In general, the regions of the leading contribution group around the states' energies, but the distributions may be asymmetric because of the presence of other states. We next turn to the distribution of single-exciton states [Fig. 10(b)]. Since the single excitons are obtained by emission from a two-exciton state, the distribution closely resembles the double-exciton distribution in Fig. 10(a). For instance, when $\omega_p \sim 22\,200\ \mathrm{cm}^{-1}$, the double-exciton state f_{11} is on resonance. It decays primarily into the single-exciton state e_5, and accordingly, the contribution of this state increases around the same value of the pump frequency. The same holds for, e.g., the double-exciton state f_{30} and the single-exciton state e_{10}. However, in most cases the different contributions overlap, and the relation between the single-exciton and the double-exciton states is more complex.

V. TWO-PHOTON-INDUCED FLUORESCENCE

Having discussed our simulations of the excited-state distribution created by entangled light, we now turn to the question whether it may be possible to detect fingerprints of these distributions in experiments. To that end, we calculate

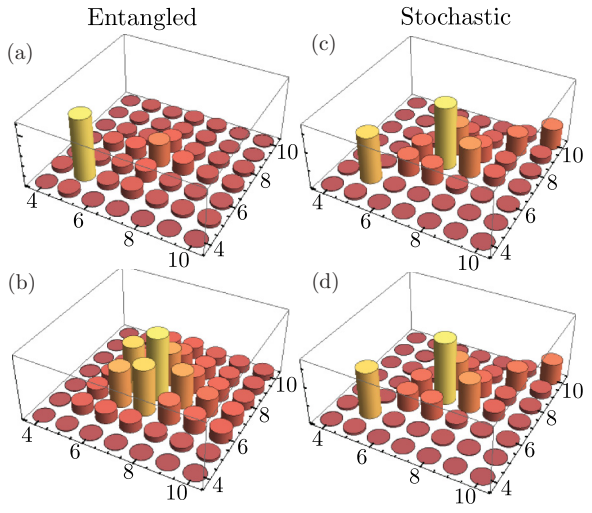

FIG. 7. (Color online) Same as Fig. 6, but for the single-exciton manifold. Only dominant states $e_4 \cdots e_{10}$ are shown.

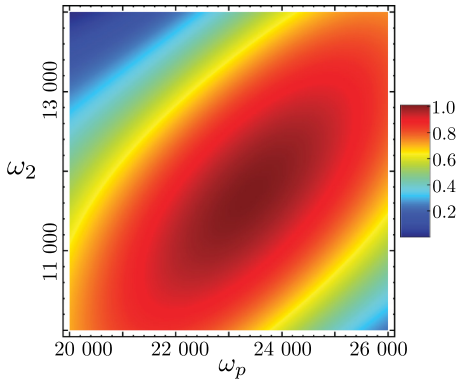

FIG. 8. (Color online) Second-order contribution to the total single-exciton manifold population $\sum_e \varrho_{ee}(t)$, Eq. (7), with $T = 30$ fs.

the dispersed fluorescence signal. This involves transitions between double- and single-exciton states as well as transitions between single-exciton states and the ground state, i.e.,

$$S_f(\omega_s;\Gamma) = \sum_{e,f} |\mu_{fe}|^2 p_f(t;\Gamma)\delta(\omega_f - \omega_e - \omega_s), \quad (23)$$

$$S_e(\omega_s;\Gamma) = \sum_{e} |\mu_{eg}|^2 p_e(t;\Gamma)\delta(\omega_e - \omega_s). \quad (24)$$

Here, ω_s is the emitted fluorescence frequency, and p_f (p_e) is the population of state f (e) given by Eq. (11) [Eq. (10)]. More elaborate detection (gated time and frequency, photon statistics) is possible [49] but will not be considered here.

In Fig. 11, we display this signal vs the pump frequency ω_p and the emission frequency ω_s. The δ functions in Eqs. (23) and (24) were replaced by a Lorentzian, which means the width of the peaks in horizontal direction of Fig. 11 is instrumental. In analogy to the populations shown in Fig. 9, the fluorescence simulation with entangled photons [Fig. 11(a)] shows two distinct resonances along the ω_p axis, pertaining to bands a and b, respectively (see also Fig. 13). Along ω_s (horizontal axis), it contains two contributions, one around $\omega_s \sim 10\,000\ \mathrm{cm}^{-1}$ and a higher-energy part between 12 000 and 13 000 cm^{-1}, reminiscent of the absorption spectrum. This pronounced structure can be exploited to enhance or suppress certain features, as will be demonstrated in the following.

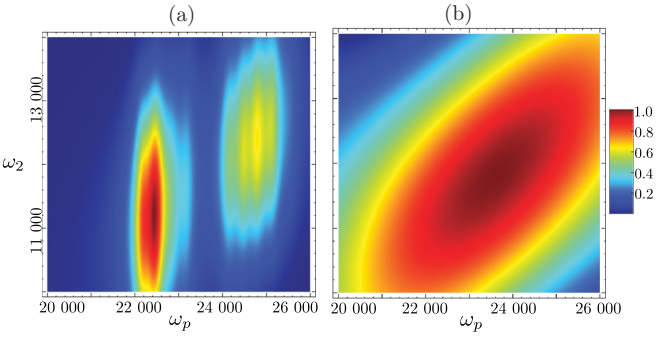

FIG. 9. (Color online) Total population of the double-exciton manifold $\sum_f \varrho_{ff}$ [Eq. (11)] plotted vs ω_2 and ω_p. (a) Excitation by entangled light with $T = 30$ fs. (b) Excitation by stochastic light.

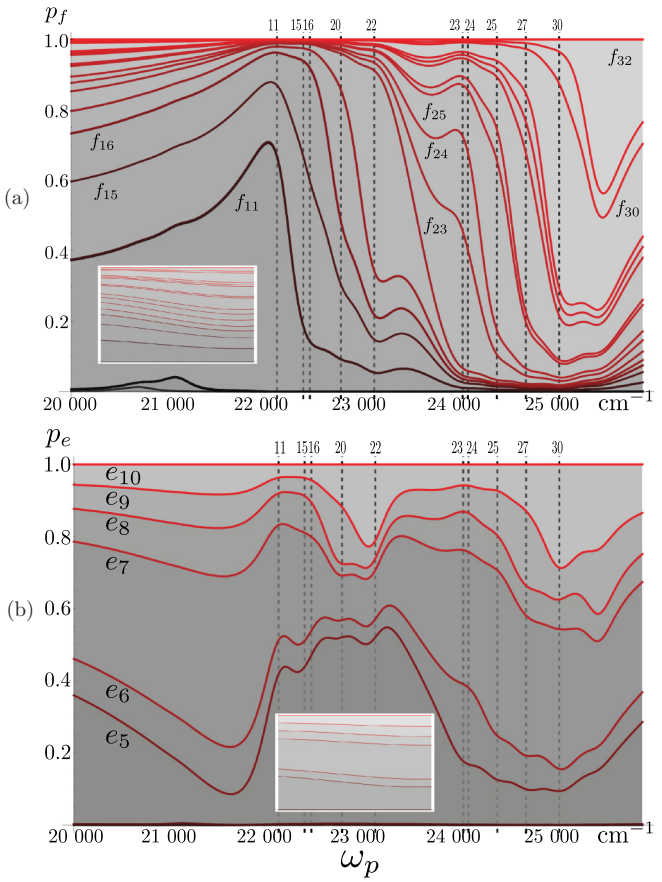

FIG. 10. (Color online) (a) Contributions of the various f states to the total population for $\omega_2 = 11\,000\ \mathrm{cm}^{-1}$, with $T = 30$ fs, upon excitation by entangled light. The inset shows the excitation by stochastic light. (b) Same for the single-exciton states.

The simulation of the stochastic signal in Fig. 11(b) shows no structure along the ω_p axis and, consequently, does not allow a manipulation of the fluorescence signal. The dispersed fluorescence simulation for $\omega_p = 22\,160\ \mathrm{cm}^{-1}$ is shown in Fig. 12(a). Most of the peaks can be directly attributed to the energy of single-exciton states; the transition thus corresponds

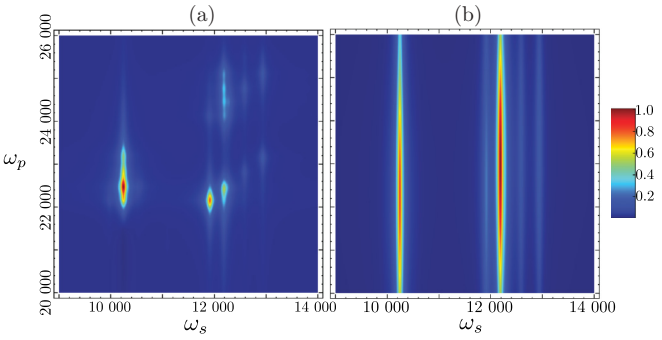

FIG. 11. (Color online) (a) Two-dimensional spectrum of the fluorescence signal of entangled photons with entanglement time $T = 30$ fs. (b) The corresponding spectrum with classical stochastic light. We set the frequency $\omega_2 = 11\,000\ \mathrm{cm}^{-1}$. Two-exciton peaks are indicated by vertical black lines, and single-exciton peaks are shown by horizontal lines.

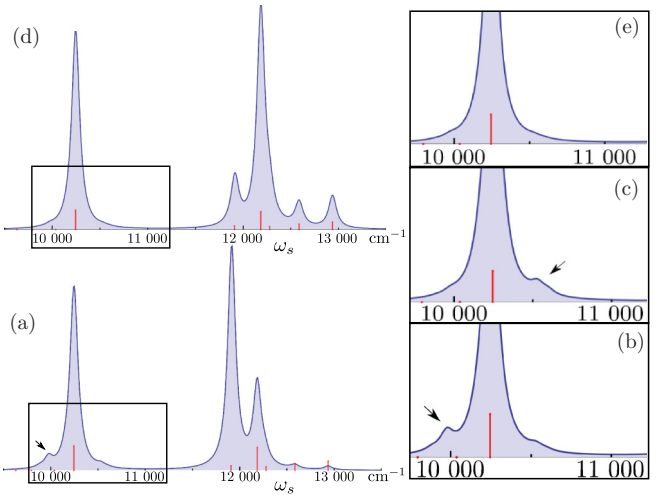

FIG. 12. (Color online) (a) The dispersed fluorescence signal induced by entangled photons with entanglement time $T = 30$ fs and $\omega_p = 22\,160\ \mathrm{cm}^{-1}$. (b) Enlarged region shown by the black box. (c) Enlarged region for $\omega_p = 22500\ \mathrm{cm}^{-1}$. (d) and (e) Same as (a) and (b), but for stochastic light.

to fluorescence either from the single-exciton manifold or from double-exciton states, whose energies closely match the sum of two single-exciton states. However, the simulations also show side peaks of the resonance at $10\,245\ \mathrm{cm}^{-1}$, which cannot be assigned to single-exciton energies. The strongest of these peaks is highlighted by the black arrow in Fig. 12(b). It corresponds to the $f_{11} \rightarrow e_7$ transition. Since state f_{11} is most strongly excited at the given pump frequency [see Fig. 10(a)], this peak is most pronounced. At pump frequency $22\,500\ \mathrm{cm}^{-1}$ resonantly excited states f_{15} and f_{16} show different transitions into the single-exciton state e_6 [see Fig. 12(c)]. The simulation with stochastic light shown in Figs. 12(d) and 12(e) cannot resolve any of these side peaks due to its broadband nature.

VI. CONCLUSIONS

We derived expressions for the single- and double-exciton density matrices of quantum systems interacting with arbitrary light sources perturbatively in the field. These were used to simulate the excitation of matter via entangled twin photons and stochastic light with the same power spectrum. Applications to the reaction center of purple bacteria show that the populations strongly depend on the nature of the light, and we indicated how these properties could be observed in the frequency-resolved fluorescence measurements. The nonclassical spectral profile of entangled light allows us to target specific double-exciton states and to explore all the excitation pathways to this state in a single shot. This shows up perspicuously in the fluorescence action spectrum in Fig. 13. The spectrum reveals the level structure of the double-exciton manifold, whereas the stochastic light cannot resolve this structure. For completeness, we also plot the action spectrum created by two cw laser beams with frequencies ω_1 and ω_2 at the peaks of the spectral density. Even though the narrow bandwidth of these beams allows for a good ω_p resolution, this signal is most pronounced when one of the laser beams

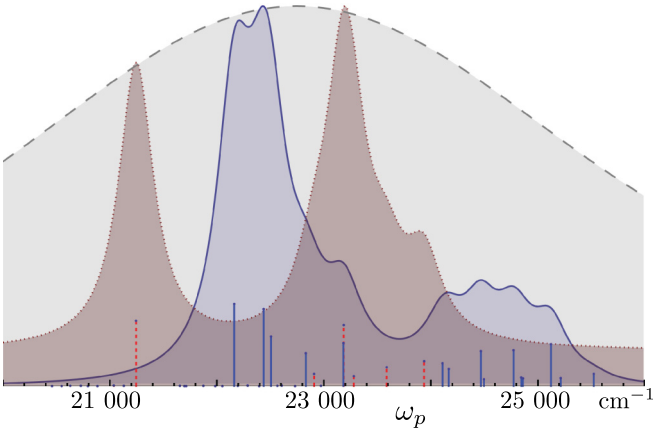

FIG. 13. (Color online) The fluorescence action spectrum (integrated over the emission frequency ω_s) vs the pump frequency ω_p: signal created by entangled photons (solid blue line), the stochastic light (dashed gray line), and signal created by two monochromatic beams at ω_1 and ω_2 (dotted red line). The double-exciton energies are plotted as vertical solid lines, and their heights are given by $|\sum_e \mu_{ge}\mu_{ef}|^2$. The single-exciton energies are indicated as vertical dashed lines, with the height proportional to $|\mu_{ge}|^2$.

is resonant with a single-exciton state, and thus it closely resembles the linear spectrum in Fig. 5.

The role of entanglement and coherent transport in the efficiency of exciton transport in photosynthetic complexes has been the subject of intense debate [50–57]. Using our formalism, one could also discuss the entanglement of quasiparticles in the double-exciton manifold [58,59]. This will require us to decompose double-exciton states into single excitons, which goes beyond the scope of the present paper.

Other possible extensions are to excitation by pulsed light and to include time and frequency gating in order to obtain control over the time and frequency resolution of the detection. The time resolution could allow us to monitor the dynamics of exciton transport and charge separation after interaction with entangled light in an experimentally feasible way.

ACKNOWLEDGMENTS

We gratefully acknowledge the support of the National Science Foundation through Grant No. CHE-1058791; the Chemical Sciences, Geosciences and Biosciences Division, Office of Basic Energy Sciences, Office of Science, US Department of Energy; and the Defense Advanced Research Projects Agency (DARPA), Grant No. UOFT-49606. B.P.F. gratefully acknowledges support from the Alexander von Humboldt Foundation through the Feodor-Lynen program.

APPENDIX A: EXCITATIONS INDUCED BY TWIN PHOTONS

Using Eq. (12), the field correlation function of the leading-order contribution, given by Eq. (7), yields

$$\langle E^\dagger(\tau_2)E(\tau_1)\rangle = C\,\mathrm{tri}\left(\frac{\tau_2-\tau_1}{T}\right)(e^{-i\omega_1(\tau_1-\tau_2)}+e^{-i\omega_2(\tau_1-\tau_2)}), \tag{A1}$$

where we have defined the triangular function

$$\mathrm{tri}(x) = \begin{cases} 1-|x| & \text{for} \quad |x|<1, \\ 0 & \text{otherwise.} \end{cases} \tag{A2}$$

Expanding the matter correlation function into a sum-over-states expression, we obtain

$$\varrho'_{e_i,e_j}(t;\Gamma) = \frac{i\mu_{ge_i}\mu_{ge_j}}{4\hbar^4(\omega_{e_ie_j}+2i\gamma_e)}\{\mathrm{sinc}[(\omega_1-\omega_{e_ig}+i\gamma_{e_i})T/2] + \mathrm{sinc}[(\omega_2-\omega_{e_jg}-i\gamma_{e_j})T/2]\}, \tag{A3}$$

where we dropped the constant factor C. The matrix element of the dipole operator connecting states g and e is denoted μ_{ge}, the energy difference is given by ω_{eg}, and the lifetime broadening is denoted by γ_e. We can assume that $\gamma_{e_i} \approx \gamma_{e_j}$. Since the entanglement time T is short relative to other time scales in the system ($T \sim 10^{-3}$ cm), this contribution to the single-exciton states depends weakly on the pump frequency ω_p.

The field correlation function of Eq. (9) can be recast as a normally ordered term plus a commutator term, which we neglect. Using Eq. (15) and dropping the constant factor C, we obtain for the populations

$$\varrho_{e,e\mathrm{I}}(t;\Gamma) = \mathrm{Re}\left\{\sum_{e,e'} T\frac{\mu_{ge}^2\mu_{ge'}^2}{\gamma_e\hbar^4}\frac{e^{i(\omega_1-\omega_{e'g}+i\gamma_{e'})T}-1}{\omega_1-\omega_{e'g}+i\gamma_{e'}} \times \frac{e^{i(\omega_2-\omega_{eg}+i\gamma_e)T}-1}{\omega_2-\omega_{eg}+i\gamma_e}\right\}. \tag{A4}$$

This contribution is proportional to the entanglement time T, reflecting the fact that in Eq. (9) the time pairs (τ_1, τ_3) and (τ_2, τ_4) are correlated. This means that the entire process has to happen within the entanglement time T. Since this time is very short with respect to other time scales in the system, $\varrho_{e,e\mathrm{I}}$ can be neglected. The only fourth-order contribution to the single-exciton manifold is thus given by Eq. (10). In a sum-over-states expression, it reads

$$\varrho_{e_i,e_j\mathrm{II}}(t;\Gamma) = \sum_{e',f}\sum_{a,b,c,d}\frac{\mu_{ge'}\mu_{e'f}}{\hbar^4}\left[\frac{\mu_{fe_i}\mu_{ge_j}}{\omega_1+\omega_2-\omega_{fg}+i\gamma_f}\frac{e^{i(\omega_a-\omega_{e_ig}+i\gamma_{e_i})T}-1}{\omega_a-\omega_{e_ig}+i\gamma_{e_i}}\frac{e^{i(\omega_b-\omega_{e'g}+i\gamma_{e'})T}-1}{\omega_1-\omega_{e'g}+i\gamma_{e'}} - \frac{\mu_{fe_j}\mu_{ge_i}}{\omega_1+\omega_2-\omega_{fg}-i\gamma_f}\frac{e^{-i(\omega_c-\omega_{e_jg}-i\gamma_{e_j})T}-1}{\omega_c-\omega_{e_jg}-i\gamma_{e_j}}\frac{e^{-i(\omega_d-\omega_{e'g}-i\gamma_{e'})T}-1}{\omega_d-\omega_{e'g}-i\gamma_{e'}}\right], \tag{A5}$$

where the summations a, b, c, and d run over ω_1 and ω_2. It is apparent that the single-exciton peaks are multiplied by phase factors of the kind $e^{i(\omega_1-\omega_{eg}+i\gamma_e)T}-1$, while the two-exciton peak is not. Additionally, taking into account

$$\frac{e^{i(\omega-\omega_{eg}+i\gamma_e)T}-1}{\omega-\omega_{eg}+i\gamma_e}\approx 2iTe^{i(\omega-\omega_{eg})T/2}\mathrm{sinc}[(\omega-\omega_{eg})T/2], \tag{A6}$$

the single-exciton peaks have a structure very similar to Eq. (A3) and depend weakly on ω_p. Thus, $\varrho_{e_i,e_j}(t)$ is dominated by the Lorentzian $1/(\omega_1+\omega_2-\omega_{fg}+i\gamma_f)$, and this in turn means that spectroscopy with entangled photons can be used to probe the two-exciton manifold of aggregates.

We further note that Eq. (11) can be recast as the product of transition amplitudes $T_{fg}(t)$, given by

$$T_{fg}(t)=\left(-\frac{i}{\hbar}\right)^2\int_{-\infty}^{t}d\tau\int_{-\infty}^{\tau}d\tau'\,\langle f(t)|V^\dagger(\tau)V^\dagger(\tau')|g\rangle\langle 0| \times E(\tau)E(\tau')|\psi\rangle \tag{A7}$$

$$=\frac{1}{\hbar^2}\sum_e\frac{\mu_{ge}\mu_{ef}}{\omega_1+\omega_2-\omega_{fg}+i\gamma_f} \times\left(\frac{e^{i(\omega_1-\omega_{eg}+i\gamma_e)T}-1}{\omega_1-\omega_{eg}+i\gamma_e}+\frac{e^{i(\omega_2-\omega_{eg}+i\gamma_e)T}-1}{\omega_2-\omega_{eg}+i\gamma_e}\right)e^{-i(\omega_1+\omega_2)t}. \tag{A8}$$

Clearly, the single-exciton resonances are suppressed, and the detuning between ω_p and the two-exciton manifold completely determines $\varrho_{f_i,f_j}(t;\Gamma)$.

APPENDIX B: ELECTRONIC EXCITATIONS WITH STOCHASTIC LIGHT

Due to the different intensity scaling of classical signals, the main contribution to the signal will arise from the leading-order contribution in Eq. (7). Since the stochastic light reproduces the spectral density of entangled light, we obtain the same result as for entangled light [see Eq. (A3)]. Additionally, one can filter out this contribution and calculate (10) and (11) to study the electronic excitations induced by higher-order interaction with stochastic light.

Using Eqs. (9), (11), and (22), the fourth-order contributions to the single-exciton manifold yield

$$\varrho_{e_i,e_j\mathrm{II}}(t;\Gamma)=\frac{1}{8\hbar^4}\sum_{a,b}\sum_{e'}\mu_{ge'}\mu_{e'f}\mathrm{sinc}^2[(\omega_a-\omega_{e'g})T/2]\mathrm{sinc}^2[(\omega_b-\omega_{fe'})T/2] \times\left[\mu_{ge_j}\mu_{fe_i}\left(\frac{1}{(\omega_{fg}-\omega_{e'g}-\omega_{e_ig}+i\gamma_f)(\omega_{fg}-\omega_{e'g}-\omega_{e_jg}-i\gamma_f)}-\frac{1}{(\omega_{e'e_j}-2i\gamma_e)(\omega_{e_je_i}-2i\gamma_e)}\right)\right. +\left.\mu_{ge_i}\mu_{fe_j}\left(\frac{1}{(\omega_{fg}-\omega_{e'g}-\omega_{e_ig}-i\gamma_f)(\omega_{fg}-\omega_{e'g}-\omega_{e_jg}+i\gamma_f)}-\frac{1}{(\omega_{e'e_i}-2i\gamma_e)(\omega_{e_ie_j}-2i\gamma_e)}\right)\right], \tag{B1}$$

$$\varrho_{f_i,f_j}(t;\Gamma)=\frac{1}{16\hbar^4}\sum_{a,b}\sum_{e,e'}\mu_{ge}\mu_{ef_i}\mu_{ge'}\mu_{e'f_j}\mathrm{sinc}^2[(\omega_a-\omega_{eg})T/2]\mathrm{sinc}^2[(\omega_b-\omega_{f_je})T/2] \times\left(\frac{1}{(\omega_{f_jg}-\omega_{eg}-\omega_{e'g}-i\gamma_f)(\omega_{f_ig}-\omega_{eg}-\omega_{e'g}+i\gamma_f)}-\frac{1}{(\omega_{e'e}+2i\gamma_e)(\omega_{f_if_j}+2i\gamma_f)}\right). \tag{B2}$$

where we neglect the small imaginary part of the sinc^2 functions. The summations a and b run over ω_1 and ω_2, and we can assume that $\gamma_{e'}\approx\gamma_e$. In comparison with the excitations induced by entangled photons, we observe that the single-exciton peaks in Eqs. (A5) and (A8) have a very similar structure to Eqs. (B1) and (B2), respectively. However, Eqs. (10) and (11) also contain Lorentzian factors that depend on $\omega_1+\omega_2$, which dominate the signal. Those resonances are replaced by a constant background contribution in the second lines of Eqs. (B1) and (B2).

[1] R. Horodecki, P. Horodecki, M. Horodecki, and K. Horodecki, Rev. Mod. Phys. **81**, 865 (2009).

[2] A. I. Lvovsky and M. G. Raymer, Rev. Mod. Phys. **81**, 299 (2009).

[3] J.-W. Pan, Z.-B. Chen, C.-Y. Lu, H. Weinfurter, A. Zeilinger, and M. Zukowski, Rev. Mod. Phys. **84**, 777 (2012).

[4] S. L. Braunstein, Nature (London) **394**, 47 (1998).

[5] S. Lloyd and S. L. Braunstein, Phys. Rev. Lett. **82**, 1784 (1999).

[6] A. N. Boto, P. Kok, D. S. Abrams, S. L. Braunstein, C. P. Williams, and J. P. Dowling, Phys. Rev. Lett. **85**, 2733 (2000).

[7] G. S. Agarwal, R. W. Boyd, E. M. Nagasako, and S. J. Bentley, Phys. Rev. Lett. **86**, 1389 (2001).

[8] M. D'Angelo, M. V. Chekhova, and Y. Shih, Phys. Rev. Lett. **87**, 013602 (2001).

[9] E. A. Sete, K. E. Dorfman, and J. P. Dowling, J. Phys. B **44**, 225504 (2011).

[10] E. S. Polzik, J. Carri, and H. J. Kimble, Phys. Rev. Lett. **68**, 3020 (1992).
[11] M. I. Kolobov and P. Kumar, Opt. Lett. **18**, 849 (1993).
[12] V. Giovannetti, S. Lloyd, and L. Maccone, Phys. Rev. Lett. **96**, 010401 (2006).
[13] M. Richter and S. Mukamel, Phys. Rev. A **83**, 063805 (2011).
[14] O. Roslyak and S. Mukamel, Phys. Rev. A **79**, 063409 (2009).
[15] H.-B. Fei, B. M. Jost, S. Popescu, B. E. A. Saleh, and M. C. Teich, Phys. Rev. Lett. **78**, 1679 (1997).
[16] B. Dayan, Phys. Rev. A **76**, 043813 (2007).
[17] M. Richter and S. Mukamel, Phys. Rev. A **82**, 013820 (2010).
[18] O. Roslyak, C. A. Marx, and S. Mukamel, Phys. Rev. A **79**, 033832 (2009).
[19] R. Kaltenbaek, J. Lavoie, D. N. Biggerstaff, and K. J. Resch, Nat. Phys. **4**, 864 (2008).
[20] D. S. Simon and A. V. Sergienko, J. Opt. Soc. Am. B **28**, 247 (2011).
[21] A. Muthukrishnan, G. S. Agarwal, and M. O. Scully, Phys. Rev. Lett. **93**, 093002 (2004).
[22] F. Milota, J. Sperling, A. Nemeth, T. Mancìal, and H. F. Kauffmann, Acc. Chem. Res. **42**, 1364 (2009).
[23] S. Mukamel, *Principles of Nonlinear Optical Spectroscopy*, Oxford Series on Optical Sciences (Oxford University Press, Oxford, 1999).
[24] S. Mukamel and S. Rahav, Adv. At. Mol. Opt. Phys. **59**, 223 (2010).
[25] M. Scully and M. Zubairy, *Quantum Optics* (Cambridge University Press, Cambridge, 1997).
[26] K. Edamatsu, G. Oohata, R. Shimizu, and T. Itoh, Nature (London) **431**, 167 (2004).
[27] R. M. Stevenson, A. J. Hudson, R. J. Young, P. Atkinson, K. Cooper, D. A. Ritchie, and A. J. Shields, Opt. Express **15**, 6507 (2007).
[28] K. Garay-Palmett, H. J. McGuinness, O. Cohen, J. S. Lundeen, R. Rangel-Rojo, A. B. U'ren, M. G. Raymer, C. J. McKinstrie, S. Radic, and I. A. Walmsley, Opt. Express **15**, 14870 (2007).
[29] K. Garay-Palmett, A. B. U'Ren, R. Rangel-Rojo, R. Evans, and S. Camacho-López, Phys. Rev. A **78**, 043827 (2008).
[30] J. Peřina, B. E. A. Saleh, and M. C. Teich, Phys. Rev. A **57**, 3972 (1998).
[31] D. T. Smithey, M. Beck, M. Belsley, and M. G. Raymer, Phys. Rev. Lett. **69**, 2650 (1992).
[32] A. Heidmann, R. J. Horowicz, S. Reynaud, E. Giacobino, C. Fabre, and G. Camy, Phys. Rev. Lett. **59**, 2555 (1987).
[33] O. Aytür and P. Kumar, Phys. Rev. Lett. **65**, 1551 (1990).
[34] B. Dayan, A. Pe'er, A. A. Friesem, and Y. Silberberg, Phys. Rev. Lett. **93**, 023005 (2004).
[35] B. Dayan, A. Pe'er, A. A. Friesem, and Y. Silberberg, Phys. Rev. Lett. **94**, 043602 (2005).
[36] D.-I. Lee and T. Goodson, J. Phys. Chem. B **110**, 25582 (2006).
[37] A. R. Guzman, M. R. Harpham, O. Suzer, M. M. Haley, and T. G. Goodson, J. Am. Chem. Soc. **132**, 7840 (2010).
[38] B. E. A. Saleh, B. M. Jost, H.-B. Fei, and M. C. Teich, Phys. Rev. Lett. **80**, 3483 (1998).
[39] J. Javanainen and P. L. Gould, Phys. Rev. A **41**, 5088 (1990).
[40] J. Deisenhofer, O. Epp, I. Sinning, and H. Michel, J. Mol. Biol. **246**, 429 (1995).
[41] B. P. Fingerhut and S. Mukamel, J. Phys. Chem. Lett. **3**, 1798 (2012).
[42] W. Holzapfel, U. Finkele, W. Kaiser, D. Oesterhelt, H. Scheer, H. U. Stilz, and W. Zinth, Proc. Natl. Acad. Sci. USA. **87**, 5168 (1990).
[43] P. Huppmann, S. Spörlein, M. Bibikova, D. Oesterhelt, J. Wachtveitl, and W. Zinth, J. Phys. Chem. A **107**, 8302 (2003).
[44] P. Hamm, K. Gray, D. Oesterhelt, R. Feick, H. Scheer, and W. Zinth, Biochim. Biophys. Acta Bioenerg. **1142**, 99 (1993).
[45] T. Tomi, Y. Shibata, Y. Ikeda, S. Taniguchi, C. Haik, N. Mataga, K. Shimada, and S. Itoh, Biochim. Biophys. Acta Bioenerg. **1767**, 22 (2007).
[46] Y. Won and R. A. Friesner, J. Phys. Chem. **92**, 2208 (1988).
[47] W. W. Parson, Z.-T. Chu, and A. Warshel, Biochim. Biophys. Acta Bioenerg. **1017**, 251 (1990).
[48] W. W. Parson, Z. T. Chu, and A. Warshel, Biophys. J. **74**, 182 (1998).
[49] K. E. Dorfman and S. Mukamel, Phys. Rev. A **86**, 013810 (2012).
[50] G. S. Engel, T. R. Calhoun, E. L. Read, T.-K. Ahn, T. Mancal, Y.-C. Cheng, R. E. Blankenship, and G. R. Fleming, Nature (London) **446**, 782 (2007).
[51] E. Collini and G. D. Scholes, Science **323**, 369 (2009).
[52] M. Mohseni, P. Rebentrost, S. Lloyd, and A. Aspuru-Guzik, J. Chem. Phys. **129**, 174106 (2008).
[53] M. B. Plenio and S. F. Huelga, New J. Phys. **10**, 113019 (2008).
[54] F. Caruso, A. W. Chin, A. Datta, S. F. Huelga, and M. B. Plenio, Phys. Rev. A **81**, 062346 (2010).
[55] T. Scholak, F. de Melo, T. Wellens, F. Mintert, and A. Buchleitner, Phys. Rev. E **83**, 021912 (2011).
[56] T. Mancal, N. Christensson, V. Luke, F. Milota, O. Bixner, H. F. Kauffmann, and J. Hauer, J. Phys. Chem. Lett. **3**, 1497 (2012).
[57] N. Christensson, H. F. Kauffmann, T. Pullerits, and T. Mancal, J. Phys. Chem. B **116**, 7449 (2012).
[58] S. Mukamel, J. Chem. Phys. **132**, 241105 (2010).
[59] F. Mintert, A. R. Carvalho, M. Kuś, and A. Buchleitner, Phys. Rep. **415**, 207 (2005).